ANNUAL REVIEWS

Annual Review of Biomedical Engineering

4D Flow with MRI

Gilles Soulat,[1] Patrick McCarthy,[2] and Michael Markl[1,3]

[1]Department of Radiology, Feinberg School of Medicine, Northwestern University, Chicago, Illinois 60611, USA; email: gilles.soulat@northwestern.edu

[2]Division of Cardiac Surgery, Department of Surgery, Feinberg School of Medicine, Northwestern University, Chicago, Illinois 60611, USA; email: Patrick.McCarthy@nm.org

[3]Department of Biomedical Engineering, McCormick School of Engineering, Northwestern University, Evanston, Illinois 60208, USA; email: mmarkl@northwestern.edu

Annu. Rev. Biomed. Eng. 2020. 22:103–26

First published as a Review in Advance on March 10, 2020

The *Annual Review of Biomedical Engineering* is online at bioeng.annualreviews.org

https://doi.org/10.1146/annurev-bioeng-100219-110055

Keywords

4D flow, magnetic resonance imaging, blood flow, hemodynamics

Abstract

Magnetic resonance imaging (MRI) has become an important tool for the clinical evaluation of patients with cardiac and vascular diseases. Since its introduction in the late 1980s, quantitative flow imaging with MRI has become a routine part of standard-of-care cardiothoracic and vascular MRI for the assessment of pathological changes in blood flow in patients with cardiovascular disease. More recently, time-resolved flow imaging with velocity encoding along all three flow directions and three-dimensional (3D) anatomic coverage (4D flow MRI) has been developed and applied to enable comprehensive 3D visualization and quantification of hemodynamics throughout the human circulatory system. This article provides an overview of the use of 4D flow applications in different cardiac and vascular regions in the human circulatory system, with a focus on using 4D flow MRI in cardiothoracic and cerebrovascular diseases.

Contents

1. INTRODUCTION

Noninvasive cardiovascular evaluation with magnetic resonance imaging (MRI) is widely used to evaluate cardiovascular disease based on both morphological and functional information. Initial applications of MRI included the assessment of cardiovascular abnormalities, such as arterial stenosis, impaired global cardiac function, and myocardial fibrosis and scarring. The past decades have seen the rise of MRI-based blood flow quantification, including the integration of flow imaging with two-dimensional (2D) phase contrast (PC) MRI into clinical guidelines and algorithms (1). More recently, the use of time-resolved 3D PC MRI with three-directional flow velocity encoding, referred to as 4D flow MRI, allows for the comprehensive in vivo measurement of 3D blood flow dynamics in the heart and large vessels, with full volumetric coverage throughout the cardiac cycle. The resulting data (3D + time + 3 velocity directions) allow for the calculation of a multitude of derived fluid mechanics parameters, such as wall shear stress (WSS), kinetic energy, and pressure gradients. The opportunity to better understand and assess in vivo 3D blood flow dynamics has made both the acquisition methods and applications of 4D flow the subject of intense ongoing research in the cardiovascular imaging community.

In this review, we focus on the most recent technical advances, in terms of both optimization of MRI data acquisition and advanced post-processing. For a description of the more standard technical aspects, the reader is referred to two 2015 consensus papers (2, 3). In addition, this article provides an overview of the use of 4D flow applications in different cardiac and vascular regions in the human circulatory system, with a focus on using 4D flow MRI in cardiothoracic and cerebrovascular diseases.

2. TECHNICAL ASPECTS

2.1. Traditional 2D Flow Imaging with MRI

PC MRI (also termed flow-sensitive MRI or MR velocity mapping) was originally described in the 1980s (4–6) and takes advantage of the direct relationship between blood flow velocity and the phase of the MRI signal. To eliminate unwanted background phase effects, two acquisitions with different velocity-dependent signal phases are needed to encode (using bipolar magnetic field

gradients) and measure blood flow velocity along a single direction. The signal intensities in the resulting phase-difference images are directly related to the blood flow velocity and can thus be used to visualize and quantify blood flow.

For cardiovascular applications, the 2D PC data are collected over multiple cardiac cycles using ECG-gated imaging to measure time-resolved pulsatile blood flow. For a standard 2D PC MRI clinical protocol, data acquisition typically includes single-direction velocity measurement orthogonal to a 2D imaging slice (through-plane encoding) and is performed during a 10–20-s breath-hold period. Following image reconstruction, 2D PC MRI yields a series of anatomic (magnitude) and flow velocity (phase-difference) images that represent the temporal changes in morphology and blood flow during the cardiac cycle.

2.2. 4D Flow MRI: Data Acquisition

In 4D flow MRI (also termed 4D PC or 3D time-resolved PC with three-directional velocity encoding), velocity is encoded along all three spatial dimensions throughout the cardiac cycle, thus providing a time-resolved 3D velocity field. As shown in **Figure 1*a***, three-directional velocity measurements can be efficiently achieved by using interleaved four-point velocity encoding (Venc), which acquires one reference image and three velocity-encoded images along three orthogonal (x, y, z) directions. Similar to 2D PC MRI, data acquisition is synchronized with the cardiac cycle, and data collection is distributed over multiple cardiac cycles using so-called k-space segmentation techniques (only a fraction of the entire 4D flow data is measured during each cardiac cycle, and the data are successively collected over multiple cardiac cycles). After completion of the 4D flow acquisition, four time-resolved 3D data sets are generated (these are magnitude data depicting anatomy and three flow data sets representing the velocities V_x, V_y, and V_z) (**Figure 1*b***). The large amount of data collected over multiple RR intervals made 4D flow MRI incompatible with use in the clinical setting prior to developments in the 1990s and 2000s (i.e., the high amplitude magnetic field gradients, phased array coils with multireceiver channels, parallel imaging). Due to the large amount of data that has to be collected (three spatial dimensions, three velocity directions, time over the cardiac cycle), total 4D flow MRI scan times may still range between 5 and 15 min (depending on heart rate, spatiotemporal resolution, and anatomic coverage). Thus, for thoracic and abdominal applications, respiration control is needed to minimize breathing artifacts. Different strategies have been applied, including the use of respiratory bellows, navigator gating, and self-gating techniques (7–11).

2.2.1. 4D flow MRI: velocity sensitivity. Venc is an important, user-defined parameter, setting the maximum flow velocity that can be acquired without velocity aliasing. When the measured blood flow velocity exceeds the acquisition setting for Venc, velocity aliasing can occur, and this is visible as a sudden change from high to low velocity within a region of flow. Thus, accurate flow visualization and quantification may be compromised unless antialiasing correction can be successfully performed. It is important to note, however, that velocity noise is directly related to Venc. Therefore, selecting a high Venc value may alleviate the issue of velocity aliasing, but it will also increase the level of velocity noise in flow velocity images. As a result, Venc should ideally be selected to be as high as needed to avoid aliasing but as low as possible to reduce velocity noise (typical settings: Venc = 150–200 cm/s in the thoracic aorta, 250–400 cm/s in an aorta with aortic valve stenosis or coarctation, or 80–120 cm/s for cerebrovascular applications). If a large imaging volume with various vessels is examined, there may be no optimal Venc setting, so the value must be chosen in accordance with the clinical question.

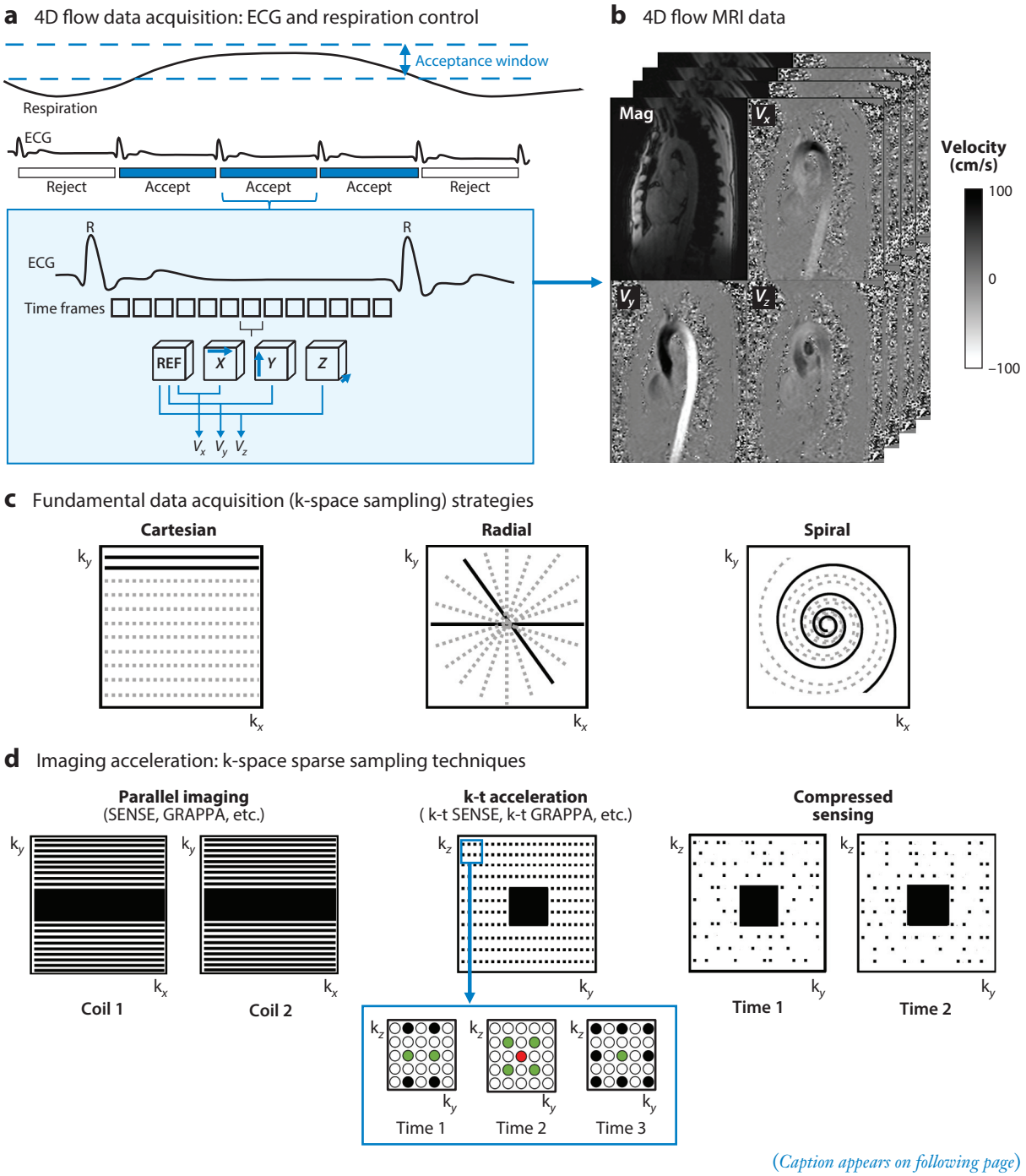

(*Caption appears on following page*)

Figure 1 (*Figure appears on preceding page*)

Data acquisition and imaging acceleration strategies used in 4D flow MRI. (*a*) Synchronization of 4D flow MRI data acquisition with cardiac motion and patient's breathing by ECG and respiratory gating. For each cardiac time frame, reference data and three velocity-sensitive scans are acquired to reconstruct four volumetric data sets. (*b*) Anatomic magnitude data and three data sets with blood flow velocities encoding along the V_x, V_y, and V_z directions. (*c*) 4D flow data can be acquired using different segmented k_x–k_y-space sampling strategies: standard Cartesian (two k-space lines collected for each cardiac cycle), radial, or spiral. (*d*) k-space undersampling techniques for 4D flow imaging acceleration. Each technique can be applied to the three sampling patterns in panel *c*. For standard parallel imaging (e.g., generalized autocalibrating partially parallel acquisition, or GRAPPA, and sensitivity encoding, or SENSE), the k-space center is fully sampled and the typically achievable acceleration factor is on the order of $R = 2$ to 3. k-t acceleration is based on sparse sampling along both the spatial and temporal dimensions, which results in higher acceleration factors, on the order of $R = 4$ to 8. 3D data are displayed for the k_z–k_y space; sampling along the temporal dimension is represented by the small graphs (*green* and *black dots* represent acquired lines). Compressed sensing is based on randomly undersampled k-space data, and the image is reconstructed using iterative techniques.

2.2.2. Acceleration techniques: k-space sampling and sparsity exploitation. Long scan times on the order of 5–15 min have previously relegated 4D flow MRI to the realm of research. However, current implementation is quickly approaching clinically feasible scan times, on the order of 2–8 min. Parallel imaging takes advantage of multichannel receiver coils, with reconstruction either in the image domain using sensitivity encoding techniques (known as SENSE) or in the k-space domain using generalized autocalibrating partially parallel acquisition (known as GRAPPA). These techniques are commonly used in MRI applications, including 4D flow, allowing a two- or threefold acceleration (**Figure 1*d***). Recently, more advanced methods such as the k-t broad-use linear acquisition speed-up technique (known as k-t BLAST) (12), k-t GRAPPA (13), k-t principal component analysis (known as k-t PCA) (14), and circular Cartesian undersampling (known as CIRCUS) (15) have allowed for even greater imaging acceleration factors (**Figure 1*d***). Another promising technique to accelerate 4D flow MRI is compressed sensing in which data are acquired in a sparse and random manner, and this is followed by nonlinear recovery of the data (16). For example, it has recently been shown that aortic 4D flow MRI with compressed sensing can be performed with scan times on the order of 2–3 min without substantial degradation of image quality (10).

Alternative techniques that are increasingly used to accelerate 4D flow MRI exploit non-Cartesian data sampling strategies, such as vastly undersampled isotropic voxel radial projection imaging (known as PC-VIPR), which uses a 3D radial sampling pattern with angular undersampling (17) or spiral data acquisition (18). Radial sampling has two advantages over Cartesian read-outs: (*a*) Sparse sampling results in streak image artifacts instead of foldover artifacts, which allows for higher undersampling factors (17); and (*b*) the center of the k-space is continuously sampled, and this results in insensitivity to a patient's motion (20). As an alternative, spiral k-space sampling can cover the entire k space uniformly and rapidly, allowing for rapid measurements of 4D flow MRI velocity (9, 11, 21). However, both radial and spiral sampling are sensitive to eddy current effects, which require efficient correction strategies, and image reconstruction is more computationally demanding (11). An illustration of acceleration techniques is provided in **Figure 1*c*,*d***.

2.3. Pre- and Post-Processing for Standard Visualization and Quantification

4D flow MRI data are affected by systematic velocity encoding errors caused by magnetic field inhomogeneity, concomitant magnetic fields (Maxwell terms), and eddy currents. Thus, data preprocessing is an important part of any data analysis workflow to correct background phase-offset errors (3). In addition, denoising and velocity antialiasing may also be applied (22).

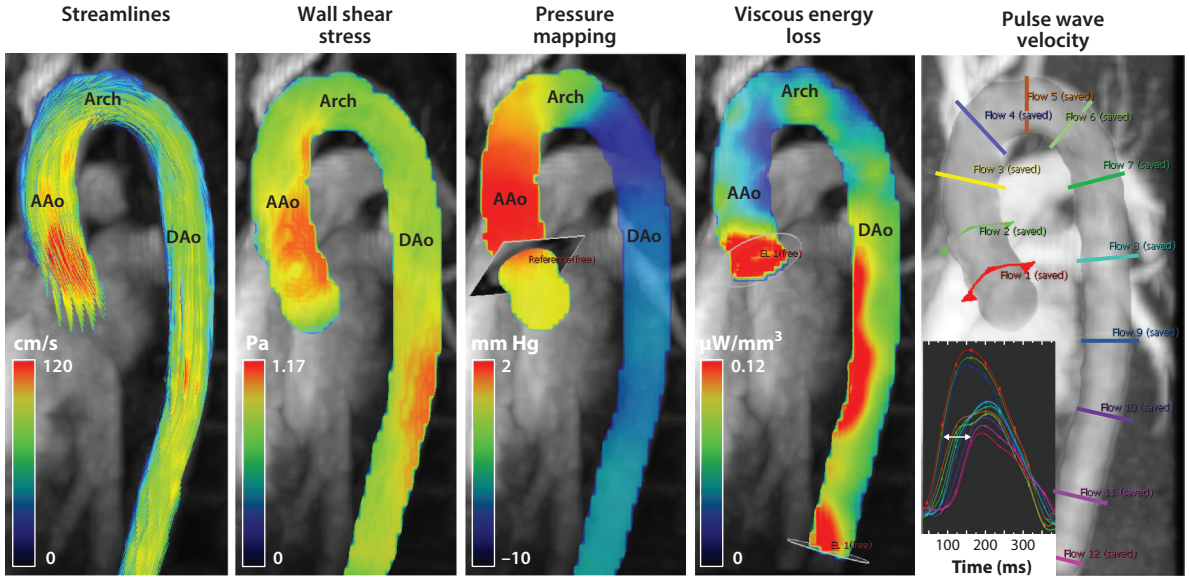

Figure 2

4D flow–based visualization of aortic hemodynamics. Example of systolic 3D streamlines, 3D wall shear stress, pressure mapping, viscous energy loss, and pulse wave velocity for a healthy aorta, all in sagittal oblique views. Abbreviations: AAo, ascending aorta; DAo, descending aorta.

After preprocessing, a 3D PC MR angiography based on a combination of magnitude and velocity data can be calculated to guide segmentation and flow visualization. Several 3D blood flow visualizing options can be employed to present the 4D flow data.

- Volumetric and maximum intensity projections of peak velocity can be used for easy volumetric identification of peak flow velocities.
- 3D streamlines represent the instantaneous blood-flow vector field for a single cardiac time frame and are used to visualize the spatial distribution and orientation of blood flow velocities. Color-coding by velocity magnitude facilitates the visual identification of regions with high systolic flow velocities (**Figure 2**).
- For visualization of the temporal evolution of 3D blood flow, time-resolved path lines can be used to display (in movie mode) the dynamic information and changes in blood flow during the cardiac cycle (3).

There are several pitfalls in 4D flow imaging that are related to the acquisition of data, the patient, and processing; **Table 1** summarizes the sources of errors and strategies for error mitigation.

2.4. Validation of Flow and Velocity Measurements

As for any novel quantitative imaging technique, validating the blood flow velocities measured by 4D flow is essential. Due to the lack of a gold standard measurement technique for the in vivo assessment of time-resolved 3D blood flow velocities inside the human body, a number of alternative approaches and surrogate validation metrics have been studied including:

- using dedicated pulsatile and steady in vitro flow phantoms (23–26)
- making comparisons with Doppler ultrasound (limited by 2D analysis planes and single-direction velocity) (27–29)

Table 1 Potential sources of errors in 4D flow MRI: types, consequences, and proposed mitigation strategies

Source of error	Type of error	Consequences	Mitigation strategy
Acquisition related	Background phase offset	Inaccurate velocities and flow	Use stationary flow fit
	Low spatial and/or temporal resolution	Underestimation of peak flow and other quantitative parameters	Adapt to the region of interest, with at least 5–6 voxels across the vessel diameter
	Inadequate Venc	Aliasing or low SNR or VNR	Set Venc to 90% of expected velocity and use unaliasing post-processing
	Inadequate FOV	Too big: acquisition time too long, resolution too low Too small: region of interest not covered, spatial aliasing	Cover region of interest
	Acceleration parameters too high	Low SNR, blurring, spatial artifacts, underestimation of velocities	Adapt parameter to sampling technique, magnetic field, coils, contrast
	Intravoxel dephasing due to turbulence	Underestimation of velocities	Increase spatial resolution, reduce echo time
Patient related	Heart rate variability	Blur	Use arrhythmia rejection algorithm, prospective gating
	Respiratory motion	Respiration artifacts (ghosting, streaks, blurring)	Use respiratory gating, soft gating, averaging
	Other motion	Blur	Work with the patient; use a shorter scan time
	Overweight	Low SNR	Use contrast
Processing related	Inadequate volumetric segmentation	Loss of measurement accuracy	Complete a visual check; provide training
	2D retrospective slice placement non-orthogonal to flow	Underestimation of velocities and flow	Use automated placement or a dedicated tool; provide training
	Inter- and intraobserver variability	Reproducibility	Use automated segmentation; provide training to observer

Abbreviations: FOV, field of view; SNR, signal-to-noise ratio; Venc, velocity encoding; VNR, velocity-to-noise ratio.

- making comparisons with standard 2D PC MRI in healthy volunteers (30–34) or patients (35–37) (limited by two analysis planes and single-direction velocity encoding)
- using internal flow consistency, based on the principle of mass conservation—that is, flow must be the same between the input and the output or between a main vessel and the sum of the branching vessels (38–40)
- making comparisons with patient-specific computational fluid dynamics (CFD), which is comparable to 4D flow because it provides representation of multidirectional volumetric velocities; several relevant studies have shown good accuracy using this comparison to quantify WSS (even if it was underestimated) and energy-derived parameters (41–43).

Studies across different institutions and MR systems have demonstrated that 4D flow MRI permits flow volume quantification that is comparable to 2D PC MRI and has good scan–rescan repeatability. Further, 4D flow MRI measures velocity in all spatial directions, has superior spatial coverage, and has been shown to be better at capturing the peak velocity of a stenotic jet (44).

2.5. Advanced Post-Processing

4D flow MRI offers the opportunity to derive advanced hemodynamic measures, such as vorticity and helicity, WSS, pressure gradients, viscous energy loss, turbulent kinetic energy, and pulse wave velocity (PWV). A more detailed description of advanced metrics is provided in **Table 2**. Some of these advanced metrics have become available in commercial software (an example of 4D flow advanced post-processing in a healthy thoracic aorta is shown in **Figure 2**), whereas most are still relegated to academic research tools.

3. APPLICATIONS

Initial applications of 4D flow MRI were focused on the heart and large vessels, such as the aorta and pulmonary arteries. Nonetheless, 4D flow MRI can be applied to other vascular territory throughout the human circulatory system, such as the cerebral large arteries and veins, carotid arteries, and abdominal (liver and renal arteries) and peripheral vessels. An overview of standard and advanced post-processing applications is provided in **Table 3** and examples are shown in **Figure 3**. In this review, we focus on the use of 4D flow MRI for the comprehensive assessment of thoracic aortic and intracranial hemodynamics.

3.1. Thoracic Aorta

Newly evolving MRI techniques such as 4D flow MRI, as well as the clinical need for continued improvements in patient diagnosis, risk stratification, and monitoring of surgical and medical treatment, have led to strong interest in applying advanced MRI techniques to diseases of the thoracic aorta. Trends in thoracic aorta MRI are moving beyond simple anatomic descriptions and aortic diameter measurements to better capture changes in aortic flow and functional impairment that result from aortic pathologies or aortic valve dysfunction.

3.1.1. Bicuspid aortic valve–related aortopathy. Bicuspid aortic valve (BAV) is a congenital fusion of the leaflets of the aortic valve affecting 1% to 2% of the general population, predominantly males. Patients with BAV have a higher risk of valve dysfunction or severe disease of the ascending aorta (dilatation, aneurysm, dissection), or both. However, the underlying mechanisms of the development of aortic disease are not fully understood, and there is ongoing debate regarding the relative contribution of genetic and hemodynamic abnormalities to BAV-associated aortopathy. 4D flow MRI–based in vivo analysis of BAV-mediated changes in aortic flow patterns has helped shed new light on the underlying mechanisms of aortopathy development in patients with BAV. 4D flow MRI studies have shown that BAV is associated with complex, disturbed blood flow dynamics when compared with those of participants with normal tricuspid aortic valves, even in the absence of aortic valve disease or aortic dilatation (45). An early 4D flow study contributed evidence that these flow alterations resulted in elevated WSS in the ascending aorta—that is, BAV patients experienced significant differences in hemodynamic forces implicated in vessel wall remodeling (46). Altered aortic WSS and flow patterns in BAV were confirmed by other studies (47, 48). Moreover, aortic WSS patterns differed based on BAV valve fusion type (49, 50) and were closely associated with the expression of different aortopathy phenotypes (51–53): Right-to-left coronary cusp fusion was associated with elevated WSS in the anterior wall, while right-to-noncoronary cusp fusion was associated with elevated WSS in the right posterior wall and aortic arch dilatation (**Figure 4**). In addition, there is a high level of evidence that WSS is mediated by valve function and is increased in cases of aortic valve stenosis (54, 55) or regurgitation (56).

Table 2 Advanced 4D flow MRI hemodynamic metrics

Metric	Equation	Description
Vorticity (ω)	$\vec{\omega} = \nabla \times \vec{v}$	Beyond visualization of flow helix using streamlines; a quantitative approach is feasible using these parameters (95–97)
Helicity	$\vec{v} \cdot \vec{\omega}$	
Wall shear stress vectors ($\vec{\tau}$)	$\vec{\tau} = 2\mu \begin{bmatrix} \frac{\partial v_x}{\partial x} & \frac{1}{2}\left(\frac{\partial v_y}{\partial x} + \frac{\partial v_y}{\partial y}\right) & \frac{1}{2}\left(\frac{\partial v_z}{\partial x} + \frac{\partial v_x}{\partial z}\right) \\ \frac{1}{2}\left(\frac{\partial v_x}{\partial y} + \frac{\partial v_y}{\partial x}\right) & \frac{\partial v_y}{\partial y} & \frac{1}{2}\left(\frac{\partial v_z}{\partial y} + \frac{\partial v_y}{\partial z}\right) \\ \frac{1}{2}\left(\frac{\partial v_x}{\partial z} + \frac{\partial v_z}{\partial x}\right) & \frac{1}{2}\left(\frac{\partial v_y}{\partial z} + \frac{\partial v_z}{\partial y}\right) & \frac{\partial v_z}{\partial z} \end{bmatrix} \cdot \vec{n}$	WSS is the blood shear rate near the vessel wall, which is implicated in endothelial changes and vascular remodeling. In 4D flow MRI, WSS can be calculated from 2D analysis planes that are perpendicular to the vessel lumen (30, 98) or, as more recently demonstrated, with 3D techniques (99–101). The oscillatory shear index is the degree of WSS inversion over the cardiac cycle. An inherent limitation of 4D flow–based WSS quantification is related to underestimation due to the relatively low spatial and temporal resolutions of 4D flow MRI compared with numerical simulations (102). Nonetheless, information about WSS distribution and relative changes have been shown to be reproducible if the 4D flow data acquisition protocol is consistent (103, 104).
Kinetic energy	$KE = \frac{1}{2} \cdot \rho \cdot V \cdot v(t)^2$	This equation for blood KE is derived from the Newtonian kinetic energy formula. The direction of the velocity is not considered in the calculation of blood KE (105).
Turbulent kinetic energy	$TKE = \frac{1}{2}\rho \sum_{i=1}^{3} \sigma_i^2$	TKE provides a direction-independent measure of flow turbulence intensity that is based on rapid velocity fluctuations within an individual imaging voxel (106).
Viscous energy loss from viscous dissipation (ϕ_v)	$\phi_v = \frac{1}{2}\sum_i \sum_j \left[\left(\frac{\partial v_i}{\partial x_j} + \frac{\partial v_j}{\partial x_i} - \frac{2}{3}(\nabla \cdot v)\delta_{ij}\right)\right]^2$, where $\delta_{ij} = 1$ for $i = j$ and $\delta_{ij} = 0$ for $i \neq j$. $EL = \mu \sum_{i=1}^{\text{num voxels}} \phi_v V_i$	Viscous energy uses the concept of viscous dissipation and is based on a reformulation of the viscous portion of the Navier–Stokes energy equations (107).
Pressure drop	$\Delta P = \frac{1}{2}\rho(v_2^2 - v_1^2) + \rho \int_1^2 \frac{dv}{dt} \cdot ds$ $\Delta P_{\text{simplified Bernoulli}} = 4v^2$	Pressure drop is a widely used clinical parameter to assess the severity of a stenosis, typically based on the simplified Bernoulli equation. In 4D flow, this concept can be expanded by taking advantage of the volumetric data set to improve estimation of the pressure drop: The extended Bernoulli equation is used to account for pressure recovery in valvular stenosis (108, 109), while the general Bernoulli equation increases the precision of pressure drop estimation (110).
Pressure mapping	$-\nabla p = \rho\left(\frac{\delta v}{\delta t} + v \cdot \nabla v - g\right) - \mu\nabla^2 v$	By assuming blood to be an incompressible laminar Newtonian fluid, pressure gradients can be calculated using the Navier–Stokes equations and displayed as 4D pressure difference maps. However, applications are challenging in cases of turbulent stenotic flow (73, 75).

(*Continued*)

Table 2 (*Continued*)

Metric	Equation	Description
Blood stasis	$r_{stasis} = \frac{n_{stasis}}{N_{tot}}$	Several methods have been proposed to quantify blood stasis based on volumetric residence time or analysis of distance traveled, following the path of a virtual particle (111) or based on low-velocity analysis in a voxel through time, with threshold values depending on the anatomic region, as in the equation proposed here (112).
Pulse wave velocity	$PWV = \frac{\Delta d}{\Delta t}$	PWV is a marker of arterial stiffness independent of blood velocities. PWV quantification requires high temporal resolution (113, 114). Changes in the method used to estimate the time shift (Δt) may induce changes in the absolute value of PWV (114).

Abbreviations: Δd, the distance traveled by the wave; EL, viscous energy loss; g, gravitational force; KE, kinetic energy; μ, blood viscosity (3.2×10^{-3} Pa); $\vec{n}$, inward normal vector; n_{stasis}, the number of cardiac time frames in the cardiac cycle below a velocity threshold (e.g., 0.1 m/s); PWV, pulse wave velocity; ρ, blood density (assumed to be 1060 kg/m^3); σ_i, velocity fluctuation intensity in three mutually perpendicular directions, i; TKE, turbulent kinetic energy; V, voxel volume; v_t, velocity magnitude for each voxel at each cardiac time frame; WSS, wall shear stress.

Recently, the application of the concept of an aorta atlas established confidence intervals for normal WSS based on results in a healthy control cohort (57, 58). This method was successfully applied to BAV patients to create WSS heat maps showing areas of increased or decreased WSS (i.e., occurring outside 95% of normal values) (59, 60) (**Figure 4**). In a prospective study with tissue collection from 20 BAV patients undergoing aortic surgery, Guzzardi et al. (61) showed a relationship between a heat map increase in WSS (>95% of normal values), extracellular matrix dysregulation (an increase in matrix metalloproteinase and transforming growth factor-β), and elastic fiber degeneration. This study demonstrated for the first time in BAV aortopathy a relationship between altered hemodynamics as assessed by 4D flow and histological wall damage. Moreover, in cases of aortic stenosis associated with BAV, elastic fiber thinning was also correlated with WSS (62).

Interestingly, a recent 4D flow MRI study found that relatives of patients with BAV who did not have aortic valve abnormalities presented with altered aortic shape and increased vortex flow (63). These results highlight the need for more data to better understand the link between the genetic disorder, the expression of the valvulopathy, and the alteration of aortic hemodynamics.

3.1.2. Marfan syndrome. Marfan syndrome is a genetic connective tissue disease with a high risk of aortic wall abnormalities that lead to aortic dilatation complicated by dissection or rupture. Disturbed blood flow patterns, such as local helix flow, have been described in the aortic root and in the proximal descending aorta (64). Circumferential WSS and peak systolic velocities were increased in patients with Marfan syndrome when compared with controls matched for degree of aortic dilatation (65). Segmental differences in WSS occurred at the inner curvature of the proximal part of the ascending aorta and in the anterior part of the more distal ascending aorta (65), while lower values were observed in the inner proximal descending aorta segment, correlating with a helix flow pattern (66). These results were confirmed in a pediatric cohort in which an inverse relationship was found between WSS and aortic diameter (67). Notably, helical flow and low WSS were found at locations known to develop aortic dissection. These findings were highlighted by the case of a patient developing a type B aortic dissection at a region of low WSS that was identified

Table 3 Overview of applications of 4D flow–derived hemodynamic parameters

Anatomic region	Disease	Parameters	References
Great vessels			
Aorta	Bicuspid-related aortopathy	FV, vorticity quantification, WSS, PWV	45, 61, 69, 96
	Marfan disease	FV, WSS, PWV	64, 65, 69
	Aneurysm or dilatation (thoracic or abdominal)	FQ, helicity quantification, EL, WSS, PWV, stasis	69, 107, 111, 115–117
	Dissection	FV, FQ	70, 71
	Coarctation	FV, pressure mapping, WSS	72, 75
	Atherosclerosis, vascular ageing	FQ, WSS, TKE, PWV, pressure mapping	118–121
	Material-related changes (graft, TEVAR)	FV, FQ, WSS	76, 82, 117
Pulmonary artery	Pulmonary hypertension	FQ, vorticity quantification, WSS, KE, EL	122–124
Cardiac			
Congenital heart	Univentricular heart treated by Fontan procedure	FV, FQ, KE, EL	125–127
	Tetralogy of Fallot	FV, FQ, vorticity quantification, KE, TKE, pressure drop	110, 128–130
	TGA treated by ASO	FV, FQ, pressure drop	110, 131
	Atrial or septal defects	FV, FQ	132, 133
Valves	Aortic stenosis	FQ, TKE, viscous energy loss, pressure drop, WSS	44, 106, 107, 134
	Aortic regurgitation	FV	135
	Mitral valve regurgitation	FV, FQ	136, 137
	Changes resulting from a valvular prosthesis	FV, WSS	138
Ventricles	Heart failure	FV, FQ, KE, TKE	139, 140
	HCM	FV, FQ, pressure drop, energy loss	141, 142
Atria and appendages	Atrial fibrillation	FV, FQ, stasis	112, 143
Small vessels			
Intracranial	Aneurysm	FV, FQ, vorticity, WSS	90
	Stenosis	FV, FQ, pressure drop	84, 85
	Malformation	FV, FQ, pressure mapping	92, 93, 144
Carotid	Stenosis	FQ, WSS	145, 146
	Atherosclerosis	PWV, WSS	147, 148
Abdominal	Portal hypertension	FV, FQ	39
	Mesenteric stenosis	FQ, WSS	149
Peripheral arteries	Stenosis	FQ, WSS	150

Abbreviations: ASO, arterial switch operation; EL, energy loss; FV, flow visualization including velocity maximum intensity projections, streamlines, and path lines to observed leakage, as well as helicity and disturbed flow; FQ, flow quantification including peak velocities, net flow, forward flow, and backward flow; HCM, hypertrophic cardiomyopathy; KE, kinetic energy; PWV, pulse wave velocity; TEVAR, thoracic endovascular aortic repair; TGA, transposition of great arteries; TKE, turbulent kinetic energy; WSS, wall shear stress.

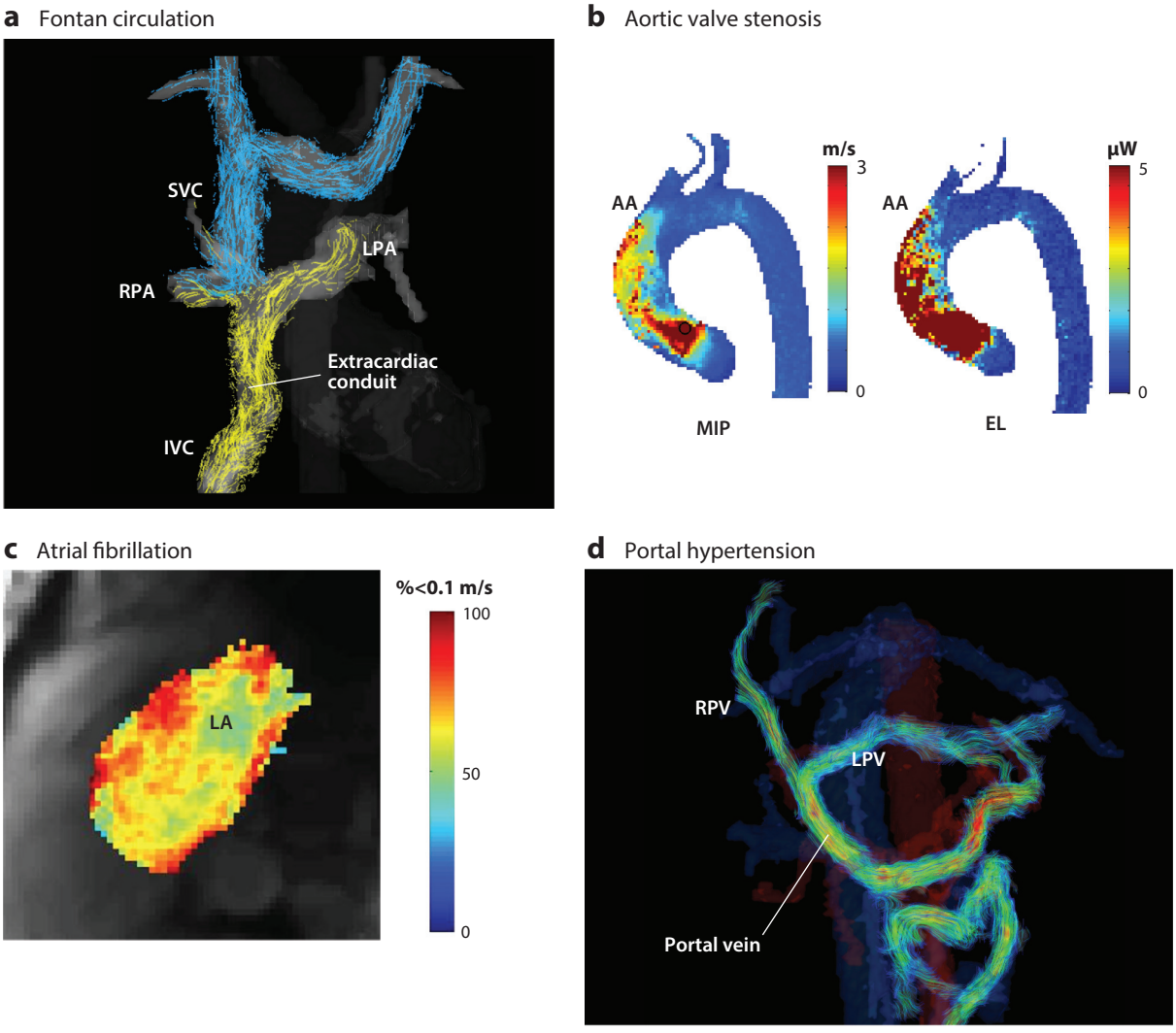

Figure 3

Example of 4D flow MRI analysis in different vascular regions. (*a*) 3D path line visualization in a 14-year-old male patient with a univentricular heart treated by Fontan surgery showing flow originating from the superior vena cava (SVC; *blue*) and the inferior vena cava (IVC) through an extracardiac conduit (*yellow*). The path lines show the relative distribution of vena cava flow in the right pulmonary artery (RPA) and left pulmonary artery (LPA). (*b*) Mapping of systolic velocity maximum intensity projection (MIP) and viscous energy loss (EL) in a 79-year-old man with aortic valve stenosis, showing a maximal velocity of 4.8 m/s and a net energy loss of 55 mW. (*c*) Flow stasis map in a dilated left atrium (LA) (210 ml maximum volume) in a patient with atrial fibrillation, with a mean stasis of 63 ± 19%. (*d*) 3D streamlines depicting liver hemodynamics and portal flow in a case of portal hypertension in a 58-year-old woman (RPV refers to the right portal vein and LPV to the left portal vein).

in a 4D flow study 3 years prior to the dissection event (68). Nonetheless, the predictive value of WSS alteration remains unclear, and further longitudinal studies are required. Another study reported increased aortic PWV (i.e., stiffness), in agreement with previous aortic distensibility studies (69).

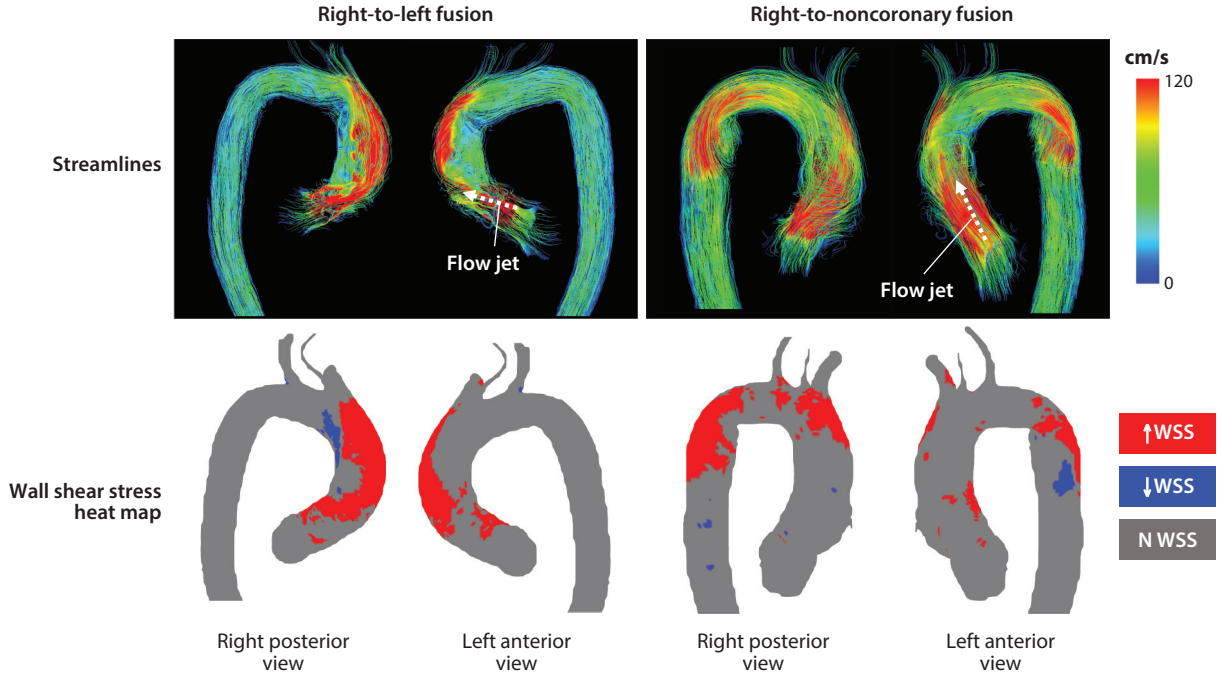

Figure 4

Aortic 4D flow MRI in bicuspid aortic valve (BAV)–related aortopathy. Wall shear stress (WSS) heat map and 3D streamline blood flow visualization in two patients with different right-to-left coronary cusp and right-to-noncoronary cusp aortic valve fusion phenotypes. (*Top*) BAV patients with right-to-left leaflet (*left*) and right-to-noncoronary (*right*) aortic valve leaflet fusion morphology. 3D streamlines at peak systole show distinct, eccentric flow jet patterns for each BAV function phenotype. (*Bottom*) 3D WSS heat maps: Red indicates regions of high WSS; blue indicates low WSS; and gray indicates normal WSS (N WSS) as compared with a healthy age- and sex-matched control cohort.

3.1.3. Aortic dissection. Aortic dissection is a life-threatening aortic wall injury leading to the creation of both a true and a false lumen. Pilot 4D flow MRI studies have been used to quantify blood flow in true and false lumens (70) and demonstrated its utility in improving the detection of hemodynamically active dissection flap tears and flow reentry sites (71).

3.1.4. Aortic coarctation. Aortic coarctation is a congenital narrowing (stenosis) of the aorta, often addressed by surgical repair in childhood. However, even after successful repair, aortic arch shape is usually altered, with an angulated aortic arch leading to marked helical flow (35), and patients often develop hypertension during follow-up. In addition, coarctation patients present with increased overall WSS (72), probably linked to both vortical and accelerated flows, even in the absence of a significant stenosis.

To assess coarctation severity, peak flow velocities at the location of the vessel narrowing (e.g., measured by Doppler echocardiography) are used to estimate the local pressure gradient via the simplified Bernoulli equation (72). A more comprehensive evaluation of pressure change in the aorta can be achieved by 4D flow–based 3D pressure mapping (73, 74). This application was validated against cardiac catheterization in a small group of patients undergoing endovascular treatment, and further studies are needed to assess its contribution to guiding the management of coarctation (75).

3.1.5. Aortic surgical or endovascular treatment. Several studies have evaluated the impact of different types of aortic valve prostheses and aortic root surgery on postintervention aortic hemodynamics. Valve-sparing aortic root replacement, mechanical valve replacement, and the Ross procedure resulted in better restoration of normal physiological flow patterns compared with the use of a bioprosthetic valve and transaortic valve replacement (76–80). However, most studies included only small sample sizes and did not control for age or aortic shape (e.g., patients undergoing transaortic valve replacement were older than those receiving surgical bioprotheses).

Following endovascular repair, 4D flow MRI may be more sensitive than computed tomography for detecting endoleaks (i.e., persistent blood flow within the aneurysm sac) (81), even without contrast injection (82), and this could be useful for preventing complications in this patient population that frequently has impaired renal function.

3.2. Intracranial Vessels

Transcranial Doppler ultrasound is routinely used for cerebrovascular flow measurements, but the technique is limited by the acoustic windows of the head. As an alternative, 4D flow MRI can be used to measure 3D cerebrovascular blood flow dynamics. Emerging applications include the hemodynamic evaluation of intracranial aneurysms, arteriovenous malformations (AVMs), and intracranial atherosclerotic disease (**Figure 5**). Of note, cerebral blood flow is highly influenced by age, and age-matched control groups are essential in clinical studies (83).

3.2.1. Intracranial atherosclerotic stenosis and vein thrombosis. Intracranial atherosclerotic plaques can alter local and global hemodynamics, particularly proximal or distal to stenosed vessels. 4D flow can be useful to estimate intracranial artery stenosis and its impact on cerebrovascular hemodynamics (**Figure 5**). In a study that included 22 patients, Wu et al. (84) found that intracranial atherosclerotic lesions altered distal flow and also altered flow in the ipsilateral collateral arteries. Pressure gradient estimation (i.e., quantification of stenosis severity) is feasible using the modified Bernoulli equation, as recently presented by Vali et al. (85) in a study of 16 patients.

In a prospective longitudinal study with 6 months of follow-up, Schuchardt et al. (86) were able to detect flow changes related to cerebral venous thrombosis, showing stagnant flow, acceleration in nonocclusive thrombosis, and change in flow directions, as well as normalization when anticoagulation treatment achieved complete recanalization.

3.2.2. Cerebral aneurysm. A large number of studies investigating flow patterns in intracranial aneurysms were based on CFD techniques used in conjunction with participant-specific boundary conditions extracted from medical images. In addition, 4D flow studies have demonstrated the feasibility of computing WSS in intracranial aneurysms in comparisons with CFD (87–89) (**Figure 5**). These studies confirmed that aneurysm size and morphology were significantly correlated with aneurysm velocity distribution, vorticity, and WSS: Saccular aneurysms had higher peak velocity than did fusiform aneurysms, while both vorticity and WSS were higher in giant saccular aneurysms compared with small saccular and fusiform aneurysms (90).

In a study including 70 unruptured cerebral aneurysms, Futami et al. (91) demonstrated that the ratio of the aneurysm to the parent vessel size (a morphological predictor of rupture) was significantly associated with inflow rate and aneurysm jet flow patterns, highlighting the potential for flow dynamics to improve stratification for rupture risk.

3.2.3. Arteriovenous malformation and fistulas. In patients with cerebral AVMs, flow information is potentially valuable for gaining a better understanding of the impact of a focal AVM

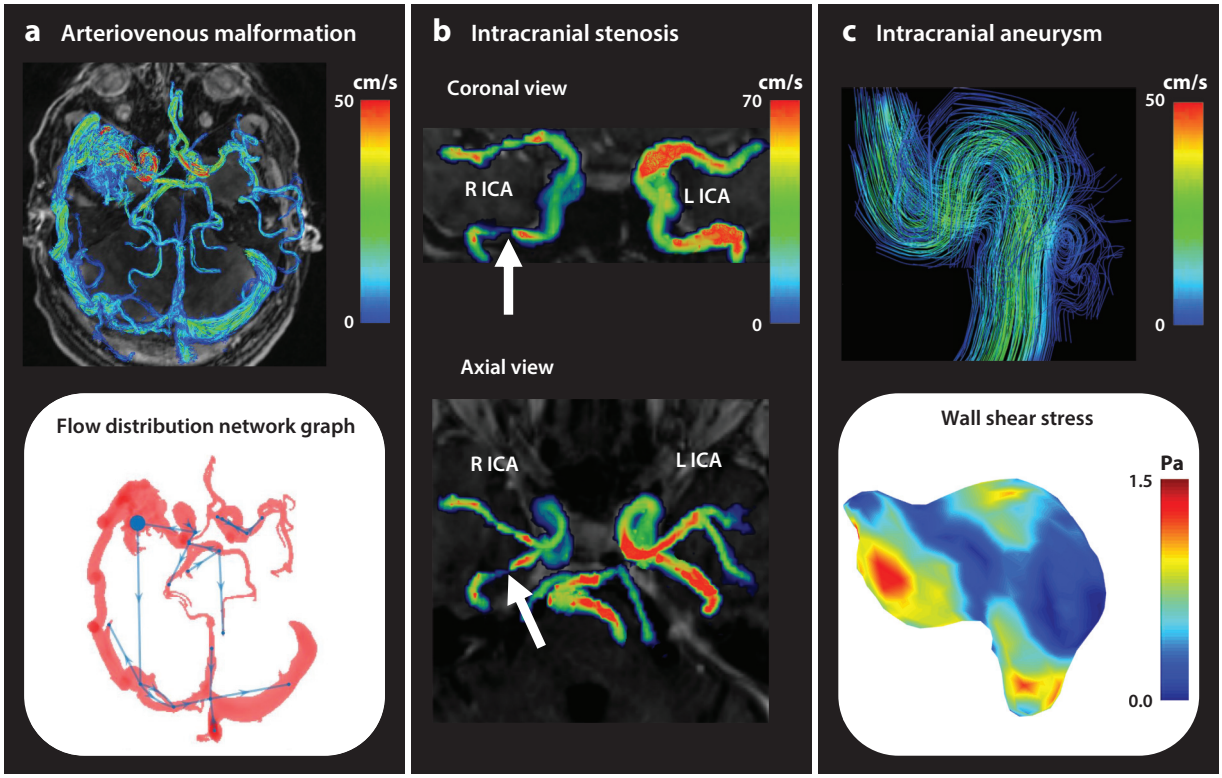

Figure 5

Intracranial 4D flow in arteriovenous malformation (AVM), intracranial artery stenosis, and aneurysm. (*a*) Spetzler–Martin grade 3 left frontal AVM in a 51-year-old male. (*Top*) 3D streamlines and (*bottom*) flow distribution network graph. (*b*) Images from a 76-year-old female with severe right intracranial carotid artery (ICA) stenosis (*white arrow*), displayed as (*top*) a velocity maximum intensity projection on coronal view and (*bottom*) axial view. Note that the maximum velocity is not seen due to a lack of temporospatial resolution even with an isotropic resolution of 1 mm^3. (*c*) Image from a 68-year-old female with a small irregular aneurysm (6 × 4 × 11 mm) with a 6-mm neck at V4 of the left vertebral artery: (*top*) streamlines and (*bottom*) wall shear stress.

on flow redistribution in the brain and guiding planning for embolization treatment. Recent studies have demonstrated the potential of 4D flow MRI for evaluating global and regional AVM flow characteristics in arteries feeding the AVM as well as in contralateral arteries and draining veins. The findings showed that 4D flow MRI could assess treatment-induced changes in cerebrovascular flow distribution and demonstrated significant associations between 4D flow metrics, cerebral perfusion indices, and AVM risk factors, such as Spetzler–Martin grade (92). To derive a better understanding of these changes in regional circle of Willis flow dynamics induced by an AVM, a systematic quantitative analysis based on a flow network graph has recently been introduced (93) (**Figure 5**).

4. FUTURE DIRECTIONS

Recent developments related to highly accelerated 4D flow MRI have resulted in increased flexibility in its application, with reduced scan times and increases in spatiotemporal resolution. These developments have led to the more widespread use of 4D flow MRI, but further improvements in spatial resolution are needed to reliably quantify vascular hemodynamics near the vessel wall

or in small arteries. Developments have also shown that the image quality of 4D flow MRI and its dynamic velocity range (e.g., fast peak systolic forward flow and slow diastolic backward flow) can be further improved by dual- or multi-Venc flow encoding. By interleaving high and low Venc acquisitions and combining these with imaging acceleration techniques, dual-Venc 4D flow MRI has shown promise for making detailed velocity measurements in neurovascular and aortic applications (23, 94).

As described in this review, many useful 4D flow MRI applications have been demonstrated, but multicenter validation and standardization are needed. Furthermore, there is a lack of outcome studies for most of the 4D flow metrics. These studies are urgently needed to prove that it has added value in the clinical setting beyond standard Doppler ultrasound or 2D PC MRI techniques. In addition, the use of 4D flow imaging has substantially expanded, but its use is mostly still limited to large academic centers, and it needs to be better integrated into the clinical workflow. To this end, efforts should focus on distributing accelerated 4D flow MRI imaging protocols and developing more efficient data analysis solutions. Current and future efforts will be dedicated to identifying the most promising 4D flow metrics, and these will be applied increasingly widely.

5. CONCLUSIONS

4D flow MRI is a technique applicable for use throughout the body, allowing for the computation of multiple hemodynamic metrics derived from a wealth of data. And there is intense ongoing research into sequence optimization, the automation of data processing, the development of new flow metrics, and continuing to expand its application to an increasing number of cardiovascular pathologies.

DISCLOSURE STATEMENT

M.M. has received research support from Siemens Healthineers, received research grants from Circle Cardiovascular Imaging and Cryolife Inc., and is a consultant for Circle Cardiovascular Imaging.

ACKNOWLEDGMENTS

The authors thank Dr. Susanne Schnell, Maria Aristova, and Justin Baraboo for their help in preparing the figures. G.S. received grant support from the French College of Radiology Teachers (CERF) and French Radiology Society (SFR).

LITERATURE CITED

1. Zoghbi WA, Adams D, Bonow RO, Enriquez-Sarano M, Foster E, et al. 2017. Recommendations for noninvasive evaluation of native valvular regurgitation: a report from the American Society of Echocardiography developed in collaboration with the Society for Cardiovascular Magnetic Resonance. *J. Am. Soc. Echocardiogr.* 30:303–71
2. Nayak KS, Nielsen JF, Bernstein MA, Markl M, Gatehouse PD, et al. 2015. Cardiovascular magnetic resonance phase contrast imaging. *J. Cardiovasc. Magn. Reson.* 17:71
3. Dyverfeldt P, Bissell M, Barker AJ, Bolger AF, Carlhall CJ, et al. 2015. 4D flow cardiovascular magnetic resonance consensus statement. *J. Cardiovasc. Magn. Reson.* 17:72
4. Moran PR. 1982. A flow velocity zeugmatographic interlace for NMR imaging in humans. *Magn. Reson. Imaging* 1:197–203
5. Nayler GL, Firmin DN, Longmore DB. 1986. Blood flow imaging by cine magnetic resonance. *J. Comput. Assist. Tomogr.* 5:715–22

6. Firmin DN, Nayler GL, Klipstein RH, Underwood SR, Rees RS, Longmore DB. 1987. In vivo validation of MR velocity imaging. *J. Comput. Assist. Tomogr.* 11:751–56
7. Bollache E, Barker AJ, Dolan RS, Carr JC, van Ooij P, et al. 2018. k-t accelerated aortic 4D flow MRI in under two minutes: feasibility and impact of resolution, k-space sampling patterns, and respiratory navigator gating on hemodynamic measurements. *Magn. Reson. Med.* 79:195–207
8. Cheng JY, Hanneman K, Zhang T, Alley MT, Lai P, et al. 2016. Comprehensive motion-compensated highly accelerated 4D flow MRI with ferumoxytol enhancement for pediatric congenital heart disease. *J. Magn. Reson. Imaging* 43:1355–68
9. Dyvorne H, Knight-Greenfield A, Jajamovich G, Besa C, Cui Y, et al. 2015. Abdominal 4D flow MR imaging in a breath hold: combination of spiral sampling and dynamic compressed sensing for highly accelerated acquisition. *Radiology* 275:245–54
10. Ma LE, Markl M, Chow K, Huh H, Forman C, et al. 2019. Aortic 4D flow MRI in 2 minutes using compressed sensing, respiratory controlled adaptive k-space reordering, and inline reconstruction. *Magn. Reson. Med.* 81:3675–90
11. Bastkowski R, Weiss K, Maintz D, Giese D. 2018. Self-gated golden-angle spiral 4D flow MRI. *Magn. Reson. Med.* 80:904–13
12. Baltes C, Kozerke S, Hansen MS, Pruessmann KP, Tsao J, Boesiger P. 2005. Accelerating cine phase-contrast flow measurements using *k-t* BLAST and *k-t* SENSE. *Magn. Reson. Med.* 54:1430–38
13. Bauer S, Markl M, Foll D, Russe M, Stankovic Z, Jung B. 2013. K-t GRAPPA accelerated phase contrast MRI: improved assessment of blood flow and 3-directional myocardial motion during breath-hold. *J. Magn. Reson. Imaging* 38:1054–62
14. Knobloch V, Boesiger P, Kozerke S. 2013. Sparsity transform k-t principal component analysis for accelerating cine three-dimensional flow measurements. *Magn. Reson. Med.* 70:53–63
15. Liu J, Koskas L, Faraji F, Kao E, Wang Y, et al. 2018. Highly accelerated intracranial 4D flow MRI: evaluation of healthy volunteers and patients with intracranial aneurysms. *Magn. Reson. Mater. Phys. Med. Biol.* 31:295–307
16. Hsiao A, Lustig M, Alley MT, Murphy M, Chan FP, et al. 2012. Rapid pediatric cardiac assessment of flow and ventricular volume with compressed sensing parallel imaging volumetric cine phase-contrast MRI. *Am. J. Roentgenol.* 198:W250–59
17. Gu T, Korosec FR, Block WF, Fain SB, Turk Q, et al. 2005. PC VIPR: a high-speed 3D phase-contrast method for flow quantification and high-resolution angiography. *Am. J. Neuroradiol.* 4:743–49
18. Sigfridsson A, Petersson S, Carlhall CJ, Ebbers T. 2012. Four-dimensional flow MRI using spiral acquisition. *Magn. Reson. Med.* 68:1065–73
19. Deleted in proof
20. Glover GH, Pauly JM. 1992. Projection reconstruction techniques for reduction of motion effects in MRI. *Magn. Reson. Med.* 28:275–89
21. Petersson S, Sigfridsson A, Dyverfeldt P, Carlhall CJ, Ebbers T. 2016. Retrospectively gated intracardiac 4D flow MRI using spiral trajectories. *Magn. Reson. Med.* 75:196–206
22. Stankovic Z, Allen BD, Garcia J, Jarvis KB, Markl M. 2014. 4D flow imaging with MRI. *Cardiovasc. Diagn. Ther.* 4:173–92
23. Nett EJ, Johnson KM, Frydrychowicz A, Del Rio AM, Schrauben E, et al. 2012. Four-dimensional phase contrast MRI with accelerated dual velocity encoding. *J. Magn. Reson. Imaging* 35:1462–71
24. Garg P, Westenberg JJM, van den Boogaard PJ, Swoboda PP, Aziz R, et al. 2018. Comparison of fast acquisition strategies in whole-heart four-dimensional flow cardiac MR: two-center, 1.5 Tesla, phantom and in vivo validation study. *J. Magn. Reson. Imaging* 47:272–81
25. Bock J, Toger J, Bidhult S, Markenroth Bloch K, Arvidsson P, et al. 2019. Validation and reproducibility of cardiovascular 4D-flow MRI from two vendors using 2 × 2 parallel imaging acceleration in pulsatile flow phantom and in vivo with and without respiratory gating. *Acta Radiol.* 60:327–37
26. Ebel S, Hubner L, Kohler B, Kropf S, Preim B, et al. 2019. Validation of two accelerated 4D flow MRI sequences at 3 T: a phantom study. *Eur. Radiol. Exp.* 3:10
27. Stankovic Z, Csatari Z, Deibert P, Euringer W, Jung B, et al. 2013. A feasibility study to evaluate splanchnic arterial and venous hemodynamics by flow-sensitive 4D MRI compared with Doppler ultrasound in patients with cirrhosis and controls. *Eur. J. Gastroenterol. Hepatol.* 25:669–75

28. Gabbour M, Schnell S, Jarvis K, Robinson JD, Markl M, Rigsby CK. 2015. 4-D flow magnetic resonance imaging: blood flow quantification compared to 2-D phase-contrast magnetic resonance imaging and Doppler echocardiography. *Pediatr. Radiol.* 45:804–13
29. Rose MJ, Jarvis K, Chowdhary V, Barker AJ, Allen BD, et al. 2016. Efficient method for volumetric assessment of peak blood flow velocity using 4D flow MRI. *J. Magn. Reson. Imaging* 44:1673–82
30. Stalder AF, Russe MF, Frydrychowicz A, Bock J, Hennig J, Markl M. 2008. Quantitative 2D and 3D phase contrast MRI: optimized analysis of blood flow and vessel wall parameters. *Magn. Reson. Med.* 60:1218–31
31. Brix L, Ringgaard S, Rasmusson A, Sorensen TS, Kim WY. 2009. Three dimensional three component whole heart cardiovascular magnetic resonance velocity mapping: comparison of flow measurements from 3D and 2D acquisitions. *J. Cardiovasc. Magn. Reson.* 11:3
32. Carlson M, Airhart N, Lopez L, Silberbach M. 2012. Moderate aortic enlargement and bicuspid aortic valve are associated with aortic dissection in Turner syndrome: report of the International Turner Syndrome Aortic Dissection Registry. *Circulation* 126:2220–26
33. Frydrychowicz A, Wieben O, Niespodzany E, Reeder SB, Johnson KM, Francois CJ. 2013. Quantification of thoracic blood flow using volumetric magnetic resonance imaging with radial velocity encoding: in vivo validation. *Investig. Radiol.* 48:819–25
34. Bollache E, van Ooij P, Powell A, Carr J, Markl M, Barker AJ. 2016. Comparison of 4D flow and 2D velocity-encoded phase contrast MRI sequences for the evaluation of aortic hemodynamics. *Int. J. Cardiovasc. Imaging* 32:1529–41
35. Hope MD, Meadows AK, Hope TA, Ordovas KG, Saloner D, et al. 2010. Clinical evaluation of aortic coarctation with 4D flow MR imaging. *J. Magn. Reson. Imaging* 31:711–18
36. Hanneman K, Sivagnanam M, Nguyen ET, Wald R, Greiser A, et al. 2014. Magnetic resonance assessment of pulmonary (Q_P) to systemic (Q_S) flows using 4D phase-contrast imaging: pilot study comparison with standard through-plane 2D phase-contrast imaging. *Acad. Radiol.* 21:1002–8
37. Valverde I, Nordmeyer S, Uribe S, Greil G, Berger F, et al. 2012. Systemic-to-pulmonary collateral flow in patients with palliated univentricular heart physiology: measurement using cardiovascular magnetic resonance 4D velocity acquisition. *J. Cardiovasc. Magn. Reson.* 14:25
38. Hsiao A, Alley MT, Massaband P, Herfkens RJ, Chan FP, Vasanawala SS. 2011. Improved cardiovascular flow quantification with time-resolved volumetric phase-contrast MRI. *Pediatr. Radiol.* 41:711–20
39. Roldan-Alzate A, Frydrychowicz A, Niespodzany E, Landgraf BR, Johnson KM, et al. 2013. In vivo validation of 4D flow MRI for assessing the hemodynamics of portal hypertension. *J. Magn. Reson. Imaging* 37:1100–8
40. Tariq U, Hsiao A, Alley M, Zhang T, Lustig M, Vasanawala SS. 2013. Venous and arterial flow quantification are equally accurate and precise with parallel imaging compressed sensing 4D phase contrast MRI. *J. Magn. Reson. Imaging* 37:1419–26
41. Isoda H, Ohkura Y, Kosugi T, Hirano M, Alley MT, et al. 2010. Comparison of hemodynamics of intracranial aneurysms between MR fluid dynamics using 3D cine phase-contrast MRI and MR-based computational fluid dynamics. *Neuroradiology* 52:913–20
42. Cibis M, Jarvis K, Markl M, Rose M, Rigsby C, et al. 2015. The effect of resolution on viscous dissipation measured with 4D flow MRI in patients with Fontan circulation: evaluation using computational fluid dynamics. *J. Biomech.* 48:2984–89
43. Szajer J, Ho-Shon K. 2018. A comparison of 4D flow MRI-derived wall shear stress with computational fluid dynamics methods for intracranial aneurysms and carotid bifurcations—a review. *Magn. Reson. Imaging* 48:62–69
44. Nordmeyer S, Riesenkampff E, Messroghli D, Kropf S, Nordmeyer J, et al. 2013. Four-dimensional velocity-encoded magnetic resonance imaging improves blood flow quantification in patients with complex accelerated flow. *J. Magn. Reson. Imaging* 37:208–16
45. Hope MD, Hope TA, Meadows AK, Ordovas KG, Urbania TH, et al. 2010. Bicuspid aortic valve: four-dimensional MR evaluation of ascending aortic systolic flow patterns. *Radiology* 255:53–61
46. Barker AJ, Lanning C, Shandas R. 2010. Quantification of hemodynamic wall shear stress in patients with bicuspid aortic valve using phase-contrast MRI. *Ann. Biomed. Eng.* 38:788–800

47. Meierhofer C, Schneider EP, Lyko C, Hutter A, Martinoff S, et al. 2013. Wall shear stress and flow patterns in the ascending aorta in patients with bicuspid aortic valves differ significantly from tricuspid aortic valves: a prospective study. *Eur. Heart J. Cardiovasc. Imaging* 14:797–804
48. Shan Y, Li J, Wang Y, Wu B, Barker AJ, et al. 2017. Aortic shear stress in patients with bicuspid aortic valve with stenosis and insufficiency. *J. Thorac. Cardiovasc. Surg.* 153:1263–72.e1
49. Barker AJ, Markl M, Burk J, Lorenz R, Bock J, et al. 2012. Bicuspid aortic valve is associated with altered wall shear stress in the ascending aorta. *Circ. Cardiovasc. Imaging* 5:457–66
50. Bissell MM, Hess AT, Biasiolli L, Glaze SJ, Loudon M, et al. 2013. Aortic dilation in bicuspid aortic valve disease: flow pattern is a major contributor and differs with valve fusion type. *Circ. Cardiovasc. Imaging* 6:499–507
51. Mahadevia R, Barker AJ, Schnell S, Entezari P, Kansal P, et al. 2014. Bicuspid aortic cusp fusion morphology alters aortic three-dimensional outflow patterns, wall shear stress, and expression of aortopathy. *Circulation* 129:673–82
52. Rodriguez-Palomares JF, Dux-Santoy L, Guala A, Kale R, Maldonado G, et al. 2018. Aortic flow patterns and wall shear stress maps by 4D-flow cardiovascular magnetic resonance in the assessment of aortic dilatation in bicuspid aortic valve disease. *J. Cardiovasc. Magn. Reson.* 20:28
53. Dux-Santoy L, Guala A, Teixido-Tura G, Ruiz-Munoz A, Maldonado G, et al. 2019. Increased rotational flow in the proximal aortic arch is associated with its dilation in bicuspid aortic valve disease. *Eur. Heart J. Cardiovasc. Imaging* 20:1407–17
54. Allen BD, van Ooij P, Barker AJ, Carr M, Gabbour M, et al. 2015. Thoracic aorta 3D hemodynamics in pediatric and young adult patients with bicuspid aortic valve. *J. Magn. Reson. Imaging* 42:954–63
55. Farag ES, van Ooij P, Planken RN, Dukker KCP, de Heer F, et al. 2018. Aortic valve stenosis and aortic diameters determine the extent of increased wall shear stress in bicuspid aortic valve disease. *J. Magn. Reson. Imaging* 48:522–30
56. Shan Y, Li J, Wang Y, Wu B, Barker AJ, et al. 2019. Aortic stenosis exacerbates flow aberrations related to the bicuspid aortic valve fusion pattern and the aortopathy phenotype. *Eur. J. Cardiothorac. Surg.* 55:534–42
57. Bustamante M, Petersson S, Eriksson J, Alehagen U, Dyverfeldt P, et al. 2015. Atlas-based analysis of 4D flow CMR: automated vessel segmentation and flow quantification. *J. Cardiovasc. Magn. Reson.* 17:87
58. Cibis M, Bustamante M, Eriksson J, Carlhall CJ, Ebbers T. 2017. Creating hemodynamic atlases of cardiac 4D flow MRI. *J. Magn. Reson. Imaging* 46:1389–99
59. van Ooij P, Potters WV, Nederveen AJ, Allen BD, Collins J, et al. 2015. A methodology to detect abnormal relative wall shear stress on the full surface of the thoracic aorta using four-dimensional flow MRI. *Magn. Reson. Med.* 73:1216–27
60. van Ooij P, Garcia J, Potters WV, Malaisrie SC, Collins JD, et al. 2016. Age-related changes in aortic 3D blood flow velocities and wall shear stress: implications for the identification of altered hemodynamics in patients with aortic valve disease. *J. Magn. Reson. Imaging* 43:1239–49
61. Guzzardi DG, Barker AJ, van Ooij P, Malaisrie SC, Puthumana JJ, et al. 2015. Valve-related hemodynamics mediate human bicuspid aortopathy: insights from wall shear stress mapping. *J. Am. Coll. Cardiol.* 66:892–900
62. Bollache E, Guzzardi DG, Sattari S, Olsen KE, Di Martino ES, et al. 2018. Aortic valve-mediated wall shear stress is heterogeneous and predicts regional aortic elastic fiber thinning in bicuspid aortic valve–associated aortopathy. *J. Thorac. Cardiovasc. Surg.* 156:2112–20.e2
63. Schnell S, Smith DA, Barker AJ, Entezari P, Honarmand AR, et al. 2016. Altered aortic shape in bicuspid aortic valve relatives influences blood flow patterns. *Eur. Heart J. Cardiovasc. Imaging* 17:1239–47
64. Geiger J, Markl M, Herzer L, Hirtler D, Loeffelbein F, et al. 2012. Aortic flow patterns in patients with Marfan syndrome assessed by flow-sensitive four-dimensional MRI. *J. Magn. Reson. Imaging* 35:594–600
65. Geiger J, Arnold R, Herzer L, Hirtler D, Stankovic Z, et al. 2013. Aortic wall shear stress in Marfan syndrome. *Magn. Reson. Med.* 70:1137–44
66. Geiger J, Hirtler D, Gottfried K, Rahman O, Bollache E, et al. 2017. Longitudinal evaluation of aortic hemodynamics in Marfan syndrome: new insights from a 4D flow cardiovascular magnetic resonance multi-year follow-up study. *J. Cardiovasc. Magn. Reson.* 19:33

67. van der Palen RL, Barker AJ, Bollache E, Garcia J, Rose MJ, et al. 2017. Altered aortic 3D hemodynamics and geometry in pediatric Marfan syndrome patients. *J. Cardiovasc. Magn. Reson.* 19:30
68. Hope TA, Kvitting JP, Hope MD, Miller DC, Markl M, Herfkens RJ. 2013. Evaluation of Marfan patients status post valve-sparing aortic root replacement with 4D flow. *Magn. Reson. Imaging* 31:1479–84
69. Guala A, Rodriguez-Palomares J, Dux-Santoy L, Teixido-Tura G, Maldonado G, et al. 2019. Influence of aortic dilation on the regional aortic stiffness of bicuspid aortic valve assessed by 4-dimensional flow cardiac magnetic resonance: comparison with Marfan syndrome and degenerative aortic aneurysm. *JACC Cardiovasc. Imaging* 12:1020–29
70. Francois CJ, Markl M, Schiebler ML, Niespodzany E, Landgraf BR, et al. 2013. Four-dimensional, flow-sensitive magnetic resonance imaging of blood flow patterns in thoracic aortic dissections. *J. Thorac. Cardiovasc. Surg.* 145:1359–66
71. Allen BD, Aouad PJ, Burris NS, Rahsepar AA, Jarvis KB, et al. 2019. Detection and hemodynamic evaluation of flap fenestrations in type B aortic dissection with 4D flow MRI: comparison with conventional MRI and CT angiography. *Radiol. Cardiothorac. Imaging* 1:e180009
72. Frydrychowicz A, Markl M, Hirtler D, Harloff A, Schlensak C, et al. 2011. Aortic hemodynamics in patients with and without repair of aortic coarctation: in vivo analysis by 4D flow-sensitive magnetic resonance imaging. *Investig. Radiol.* 46:317–25
73. Bock J, Frydrychowicz A, Lorenz R, Hirtler D, Barker AJ, et al. 2011. In vivo noninvasive 4D pressure difference mapping in the human aorta: phantom comparison and application in healthy volunteers and patients. *Magn. Reson. Med.* 66:1079–88
74. Rengier F, Delles M, Eichhorn J, Azad YJ, von Tengg-Kobligk H, et al. 2015. Noninvasive 4D pressure difference mapping derived from 4D flow MRI in patients with repaired aortic coarctation: comparison with young healthy volunteers. *Int. J. Cardiovasc. Imaging* 31:823–30
75. Riesenkampff E, Fernandes JF, Meier S, Goubergrits L, Kropf S, et al. 2014. Pressure fields by flow-sensitive, 4D, velocity-encoded CMR in patients with aortic coarctation. *JACC Cardiovasc. Imaging* 7:920–26
76. Semaan E, Markl M, Malaisrie SC, Barker A, Allen B, et al. 2014. Haemodynamic outcome at four-dimensional flow magnetic resonance imaging following valve-sparing aortic root replacement with tricuspid and bicuspid valve morphology. *Eur. J. Cardiothorac. Surg.* 45:818–25
77. Bissell MM, Loudon M, Hess AT, Stoll V, Orchard E, et al. 2018. Differential flow improvements after valve replacements in bicuspid aortic valve disease: a cardiovascular magnetic resonance assessment. *J. Cardiovasc. Magn. Reson.* 20:10
78. Farag ES, Vendrik J, van Ooij P, Poortvliet QL, van Kesteren F, et al. 2019. Transcatheter aortic valve replacement alters ascending aortic blood flow and wall shear stress patterns: a 4D flow MRI comparison with age-matched, elderly controls. *Eur. Radiol.* 29:1444–51
79. Keller EJ, Malaisrie SC, Kruse J, McCarthy PM, Carr JC, et al. 2016. Reduction of aberrant aortic haemodynamics following aortic root replacement with a mechanical valved conduit. *Interact. Cardiovasc. Thorac. Surg.* 23:416–23
80. van Kesteren F, Wollersheim LW, Baan J Jr., Nederveen AJ, Kaya A, et al. 2018. Four-dimensional flow MRI of stented versus stentless aortic valve bioprostheses. *Eur. Radiol.* 28:257–64
81. Sakata M, Takehara Y, Katahashi K, Sano M, Inuzuka K, et al. 2016. Hemodynamic analysis of endoleaks after endovascular abdominal aortic aneurysm repair by using 4-dimensional flow-sensitive magnetic resonance imaging. *Circ. J.* 80:1715–25
82. Salehi Ravesh M, Langguth P, Pfarr JA, Schupp J, Trentmann J, et al. 2019. Non-contrast-enhanced magnetic resonance imaging for visualization and quantification of endovascular aortic prosthesis, their endoleaks and aneurysm sacs at 1.5T. *Magn. Reson. Imaging* 60:164–72
83. Wu C, Honarmand AR, Schnell S, Kuhn R, Schoeneman SE, et al. 2016. Age-related changes of normal cerebral and cardiac blood flow in children and adults aged 7 months to 61 years. *J. Am. Heart Assoc.* 5:e002657
84. Wu C, Schnell S, Vakil P, Honarmand AR, Ansari SA, et al. 2017. In vivo assessment of the impact of regional intracranial atherosclerotic lesions on brain arterial 3D hemodynamics. *Am. J. Neuroradiol.* 38:515–22

85. Vali A, Aristova M, Vakil P, Abdalla R, Prabhakaran S, et al. 2019. Semi-automated analysis of 4D flow MRI to assess the hemodynamic impact of intracranial atherosclerotic disease. *Magn. Reson. Med.* 82:749–62
86. Schuchardt F, Hennemuth A, Schroeder L, Meckel S, Markl M, et al. 2017. Acute cerebral venous thrombosis: three-dimensional visualization and quantification of hemodynamic alterations using 4-dimensional flow magnetic resonance imaging. *Stroke* 48:671–77
87. Meckel S, Stalder AF, Santini F, Radu EW, Rufenacht DA, et al. 2008. In vivo visualization and analysis of 3-D hemodynamics in cerebral aneurysms with flow-sensitized 4-D MR imaging at 3 T. *Neuroradiology* 50:473–84
88. Boussel L, Rayz V, Martin A, Acevedo-Bolton G, Lawton MT, et al. 2009. Phase-contrast magnetic resonance imaging measurements in intracranial aneurysms in vivo of flow patterns, velocity fields, and wall shear stress: comparison with computational fluid dynamics. *Magn. Reson. Med.* 61:409–17
89. Isoda H, Ohkura Y, Kosugi T, Hirano M, Takeda H, et al. 2010. In vivo hemodynamic analysis of intracranial aneurysms obtained by magnetic resonance fluid dynamics (MRFD) based on time-resolved three-dimensional phase-contrast MRI. *Neuroradiology* 52:921–28
90. Schnell S, Ansari SA, Vakil P, Wasielewski M, Carr ML, et al. 2014. Three-dimensional hemodynamics in intracranial aneurysms: influence of size and morphology. *J. Magn. Reson. Imaging* 39:120–31
91. Futami K, Nambu I, Kitabayashi T, Sano H, Misaki K, et al. 2017. Inflow hemodynamics evaluated by using four-dimensional flow magnetic resonance imaging and the size ratio of unruptured cerebral aneurysms. *Neuroradiology* 59:411–18
92. Wu C, Ansari SA, Honarmand AR, Vakil P, Hurley MC, et al. 2015. Evaluation of 4D vascular flow and tissue perfusion in cerebral arteriovenous malformations: influence of Spetzler-Martin grade, clinical presentation, and AVM risk factors. *Am. J. Neuroradiol.* 36:1142–49
93. Aristova M, Vali A, Ansari SA, Shaibani A, Alden TD, et al. 2019. Standardized evaluation of cerebral arteriovenous malformations using flow distribution network graphs and dual-*venc* 4D flow MRI. *J. Magn. Reson. Imaging* 50(6):1718–30
94. Schnell S, Ansari SA, Wu C, Garcia J, Murphy IG, et al. 2017. Accelerated dual-*venc* 4D flow MRI for neurovascular applications. *J. Magn. Reson. Imaging* 46:102–14
95. Morbiducci U, Ponzini R, Rizzo G, Cadioli M, Esposito A, et al. 2011. Mechanistic insight into the physiological relevance of helical blood flow in the human aorta: an in vivo study. *Biomech. Model. Mechanobiol.* 3:339–55
96. Garcia J, Barker AJ, Collins JD, Carr JC, Markl M. 2017. Volumetric quantification of absolute local normalized helicity in patients with bicuspid aortic valve and aortic dilatation. *Magn. Reson. Med.* 78:689–701
97. Sotelo J, Urbina J, Valverde I, Mura J, Tejos C, et al. 2018. Three-dimensional quantification of vorticity and helicity from 3D cine PC-MRI using finite-element interpolations. *Magn. Reson. Med.* 79:541–53
98. Frydrychowicz A, Stalder AF, Russe MF, Bock J, Bauer S, et al. 2009. Three-dimensional analysis of segmental wall shear stress in the aorta by flow-sensitive four-dimensional-MRI. *J. Magn. Reson. Imaging* 30:77–84
99. Potters WV, van Ooij P, Marquering H, vanBavel E, Nederveen AJ. 2015. Volumetric arterial wall shear stress calculation based on cine phase contrast MRI. *J. Magn. Reson. Imaging* 41:505–16
100. van Ooij P, Potters WV, Collins J, Carr M, Carr J, et al. 2015. Characterization of abnormal wall shear stress using 4D flow MRI in human bicuspid aortopathy. *Ann. Biomed. Eng.* 43:1385–97
101. Sotelo J, Dux-Santoy L, Guala A, Rodriguez-Palomares J, Evangelista A, et al. 2018. 3D axial and circumferential wall shear stress from 4D flow MRI data using a finite element method and a laplacian approach. *Magn. Reson. Med.* 79:2816–23
102. Petersson S, Dyverfeldt P, Ebbers T. 2012. Assessment of the accuracy of MRI wall shear stress estimation using numerical simulations. *J. Magn. Reson. Imaging* 36:128–38
103. Markl M, Wallis W, Harloff A. 2011. Reproducibility of flow and wall shear stress analysis using flow-sensitive four-dimensional MRI. *J. Magn. Reson. Imaging* 33:988–94

104. van Ooij P, Powell AL, Potters WV, Carr JC, Markl M, Barker AJ. 2016. Reproducibility and interobserver variability of systolic blood flow velocity and 3D wall shear stress derived from 4D flow MRI in the healthy aorta. *J. Magn. Reson. Imaging* 43:236–48
105. Carlsson M, Heiberg E, Toger J, Arheden H. 2012. Quantification of left and right ventricular kinetic energy using four-dimensional intracardiac magnetic resonance imaging flow measurements. *Am. J. Physiol. Heart Circ. Physiol.* 302:H893–900
106. Dyverfeldt P, Hope MD, Tseng EE, Saloner D. 2013. Magnetic resonance measurement of turbulent kinetic energy for the estimation of irreversible pressure loss in aortic stenosis. *JACC Cardiovasc. Imaging* 6:64–71
107. Barker AJ, van Ooij P, Bandi K, Garcia J, Albaghdadi M, et al. 2014. Viscous energy loss in the presence of abnormal aortic flow. *Magn. Reson. Med.* 72:620–28
108. Garcia D, Dumesnil JG, Durand L-G, Kadem L, Pibarot P. 2003. Discrepancies between catheter and Doppler estimates of valve effective orifice area can be predicted from the pressure recovery phenomenon. *J. Am. Coll. Cardiol.* 41:435–42
109. Ha H, Kvitting JP, Dyverfeldt P, Ebbers T. 2019. Validation of pressure drop assessment using 4D flow MRI-based turbulence production in various shapes of aortic stenoses. *Magn. Reson. Med.* 81:893–906
110. Falahatpisheh A, Rickers C, Gabbert D, Heng EL, Stalder A, et al. 2016. Simplified Bernoulli's method significantly underestimates pulmonary transvalvular pressure drop. *J. Magn. Reson. Imaging* 43:1313–19
111. Ziegler M, Welander M, Lantz J, Lindenberger M, Bjarnegard N, et al. 2019. Visualizing and quantifying flow stasis in abdominal aortic aneurysms in men using 4D flow MRI. *Magn. Reson. Imaging* 57:103–10
112. Markl M, Lee DC, Furiasse N, Carr M, Foucar C, et al. 2016. Left atrial and left atrial appendage 4D blood flow dynamics in atrial fibrillation. *Circ. Cardiovasc. Imaging* 9:e004984
113. Markl M, Wallis W, Brendecke S, Simon J, Frydrychowicz A, Harloff A. 2010. Estimation of global aortic pulse wave velocity by flow-sensitive 4D MRI. *Magn. Reson. Med.* 63:1575–82
114. Dyverfeldt P, Ebbers T, Lanne T. 2014. Pulse wave velocity with 4D flow MRI: systematic differences and age-related regional vascular stiffness. *Magn. Reson. Imaging* 32:1266–71
115. Garcia J, Barker AJ, van Ooij P, Schnell S, Puthumana J, et al. 2015. Assessment of altered three-dimensional blood characteristics in aortic disease by velocity distribution analysis. *Magn. Reson. Med.* 74:817–25
116. Kolipaka A, Illapani VS, Kalra P, Garcia J, Mo X, et al. 2017. Quantification and comparison of 4D-flow MRI-derived wall shear stress and MRE-derived wall stiffness of the abdominal aorta. *J. Magn. Reson. Imaging* 45:771–78
117. Bollache E, Fedak PWM, van Ooij P, Rahman O, Malaisrie SC, et al. 2018. Perioperative evaluation of regional aortic wall shear stress patterns in patients undergoing aortic valve and/or proximal thoracic aortic replacement. *J. Thorac. Cardiovasc. Surg.* 155:2277–86.e2
118. Markl M, Brendecke SM, Simon J, Barker AJ, Weiller C, Harloff A. 2013. Co-registration of the distribution of wall shear stress and 140 complex plaques of the aorta. *Magn. Reson. Imaging* 31:1156–62
119. Ha H, Ziegler M, Welander M, Bjarnegard N, Carlhall CJ, et al. 2018. Age-related vascular changes affect turbulence in aortic blood flow. *Front. Physiol.* 9:36
120. Harloff A, Mirzaee H, Lodemann T, Hagenlocher P, Wehrum T, et al. 2018. Determination of aortic stiffness using 4D flow cardiovascular magnetic resonance—a population-based study. *J. Cardiovasc. Magn. Reson.* 20:43
121. Bouaou K, Bargiotas I, Dietenbeck T, Bollache E, Soulat G, et al. 2019. Analysis of aortic pressure fields from 4D flow MRI in healthy volunteers: associations with age and left ventricular remodeling. *J. Magn. Reson. Imaging* 50:982–93
122. Reiter G, Reiter U, Kovacs G, Olschewski H, Fuchsjäger M. 2015. Blood flow vortices along the main pulmonary artery measured with MR imaging for diagnosis of pulmonary hypertension. *Radiology* 275:71–79
123. Barker AJ, Roldan-Alzate A, Entezari P, Shah SJ, Chesler NC, et al. 2015. Four-dimensional flow assessment of pulmonary artery flow and wall shear stress in adult pulmonary arterial hypertension: results from two institutions. *Magn. Reson. Med.* 73:1904–13

124. Han QJ, Witschey WR, Fang-Yen CM, Arkles JS, Barker AJ, et al. 2015. Altered right ventricular kinetic energy work density and viscous energy dissipation in patients with pulmonary arterial hypertension: a pilot study using 4D flow MRI. *PLOS ONE* 10:e0138365
125. Jarvis K, Schnell S, Barker AJ, Garcia J, Lorenz R, et al. 2016. Evaluation of blood flow distribution asymmetry and vascular geometry in patients with Fontan circulation using 4-D flow MRI. *Pediatr. Radiol.* 46:1507–19
126. Rijnberg FM, Hazekamp MG, Wentzel JJ, de Koning PJH, Westenberg JJM, et al. 2018. Energetics of blood flow in cardiovascular disease: concept and clinical implications of adverse energetics in patients with a Fontan circulation. *Circulation* 137:2393–407
127. Kamphuis VP, Elbaz MSM, van den Boogaard PJ, Kroft LJM, van der Geest RJ, et al. 2019. Disproportionate intraventricular viscous energy loss in Fontan patients: analysis by 4D flow MRI. *Eur. Heart J. Cardiovasc. Imaging* 20:323–33
128. François CJ, Srinivasan S, Schiebler ML, Reeder SB, Niespodzany E, et al. 2012. 4D cardiovascular magnetic resonance velocity mapping of alterations of right heart flow patterns and main pulmonary artery hemodynamics in tetralogy of Fallot. *J. Cardiovasc. Magn. Reson.* 14:16
129. Sjoberg P, Bidhult S, Bock J, Heiberg E, Arheden H, et al. 2018. Disturbed left and right ventricular kinetic energy in patients with repaired tetralogy of Fallot: pathophysiological insights using 4D-flow MRI. *Eur. Radiol.* 28:4066–76
130. Robinson JD, Rose MJ, Joh M, Jarvis K, Schnell S, et al. 2019. 4-D flow magnetic-resonance-imaging-derived energetic biomarkers are abnormal in children with repaired tetralogy of Fallot and associated with disease severity. *Pediatr. Radiol.* 49:308–17
131. Jarvis K, Vonder M, Barker AJ, Schnell S, Rose M, et al. 2016. Hemodynamic evaluation in patients with transposition of the great arteries after the arterial switch operation: 4D flow and 2D phase contrast cardiovascular magnetic resonance compared with Doppler echocardiography. *J. Cardiovasc. Magn. Reson.* 18:59
132. Calkoen EE, Elbaz MS, Westenberg JJ, Kroft LJ, Hazekamp MG, et al. 2015. Altered left ventricular vortex ring formation by 4-dimensional flow magnetic resonance imaging after repair of atrioventricular septal defects. *J. Thorac. Cardiovasc. Surg.* 150:1233–40.e1
133. Hsiao A, Lustig M, Alley MT, Murphy MJ, Vasanawala SS. 2012. Evaluation of valvular insufficiency and shunts with parallel-imaging compressed-sensing 4D phase-contrast MR imaging with stereoscopic 3D velocity-fusion volume-rendered visualization. *Radiology* 265:87–95
134. van Ooij P, Markl M, Collins JD, Carr JC, Rigsby C, et al. 2017. Aortic valve stenosis alters expression of regional aortic wall shear stress: new insights from a 4-dimensional flow magnetic resonance imaging study of 571 subjects. *J. Am. Heart Assoc.* 6:e005959
135. Chelu RG, van den Bosch AE, van Kranenburg M, Hsiao A, van den Hoven AT, et al. 2016. Qualitative grading of aortic regurgitation: a pilot study comparing CMR 4D flow and echocardiography. *Int. J. Cardiovasc. Imaging* 32:301–7
136. Feneis JF, Kyubwa E, Atianzar K, Cheng JY, Alley MT, et al. 2018. 4D flow MRI quantification of mitral and tricuspid regurgitation: reproducibility and consistency relative to conventional MRI. *J. Magn. Reson. Imaging* 48:1147–58
137. Gorodisky L, Agmon Y, Porat M, Abadi S, Lessick J. 2018. Assessment of mitral regurgitation by 3-dimensional proximal flow convergence using magnetic resonance imaging: comparison with echo-Doppler. *Int. J. Cardiovasc. Imaging* 34:793–802
138. von Knobelsdorff-Brenkenhoff F, Trauzeddel RF, Barker AJ, Gruettner H, Markl M, Schulz-Menger J. 2014. Blood flow characteristics in the ascending aorta after aortic valve replacement—a pilot study using 4D-flow MRI. *Int. J. Cardiol.* 170:426–33
139. Eriksson J, Bolger AF, Ebbers T, Carlhall CJ. 2013. Four-dimensional blood flow–specific markers of LV dysfunction in dilated cardiomyopathy. *Eur. Heart J. Cardiovasc. Imaging* 14:417–24
140. Garg P, Crandon S, Swoboda PP, Fent GJ, Foley JRJ, et al. 2018. Left ventricular blood flow kinetic energy after myocardial infarction—insights from 4D flow cardiovascular magnetic resonance. *J. Cardiovasc. Magn. Reson.* 20:61

141. Allen BD, Choudhury L, Barker AJ, van Ooij P, Collins JD, et al. 2015. Three-dimensional haemodynamics in patients with obstructive and non-obstructive hypertrophic cardiomyopathy assessed by cardiac magnetic resonance. *Eur. Heart J. Cardiovasc. Imaging* 16:29–36
142. van Ooij P, Allen BD, Contaldi C, Garcia J, Collins J, et al. 2016. 4D flow MRI and T_1-mapping: assessment of altered cardiac hemodynamics and extracellular volume fraction in hypertrophic cardiomyopathy. *J. Magn. Reson. Imaging* 43:107–14
143. Fluckiger JU, Goldberger JJ, Lee DC, Ng J, Lee R, et al. 2013. Left atrial flow velocity distribution and flow coherence using four-dimensional FLOW MRI: a pilot study investigating the impact of age and pre- and postintervention atrial fibrillation on atrial hemodynamics. *J. Magn. Reson. Imaging* 38:580–87
144. Rivera-Rivera LA, Johnson KM, Turski PA, Wieben O. 2018. Pressure mapping and hemodynamic assessment of intracranial dural sinuses and dural arteriovenous fistulas with 4D flow MRI. *Am. J. Neuroradiol.* 39:485–87
145. Harloff A, Berg S, Barker AJ, Schollhorn J, Schumacher M, et al. 2013. Wall shear stress distribution at the carotid bifurcation: influence of eversion carotid endarterectomy. *Eur. Radiol.* 23:3361–69
146. Harloff A, Zech T, Wegent F, Strecker C, Weiller C, Markl M. 2013. Comparison of blood flow velocity quantification by 4D flow MR imaging with ultrasound at the carotid bifurcation. *Am. J. Neuroradiol.* 34:1407–13
147. Peper ES, Strijkers GJ, Gazzola K, Potters WV, Motaal AG, et al. 2018. Regional assessment of carotid artery pulse wave velocity using compressed sensing accelerated high temporal resolution 2D CINE phase contrast cardiovascular magnetic resonance. *J. Cardiovasc. Magn. Reson.* 20:86
148. van Ooij P, Cibis M, Rowland EM, Vernooij MW, van der Lugt A, et al. 2018. Spatial correlations between MRI-derived wall shear stress and vessel wall thickness in the carotid bifurcation. *Eur. Radiol. Exp.* 2:27
149. Siedek F, Giese D, Weiss K, Ekdawi S, Brinkmann S, et al. 2018. 4D flow MRI for the analysis of celiac trunk and mesenteric artery stenoses. *Magn. Reson. Imaging* 53:52–62
150. Galizia MS, Barker A, Liao Y, Collins J, Carr J, et al. 2014. Wall morphology, blood flow and wall shear stress: MR findings in patients with peripheral artery disease. *Eur. Radiol.* 24:850–56

Annual Review
of Biomedical
Engineering

Volume 22, 2020

Contents

Errata

An online log of corrections to *Annual Review of Biomedical Engineering* articles may be found at http://www.annualreviews.org/errata/bioeng